A geometrically-amplified in-plane piezoelectric actuator for mesoscale robotic systems

Peter A. York, *Student Member, IEEE,* and Robert J. Wood, *Senior Member, IEEE,*

Abstract— **Piezoelectric materials are an attractive option for electromechanical transduction on the mesoscale due to their intrinsic high force production, large bandwidth, and favorable scaling characteristics. However, the small displacements they inherently produce are typically too small to be directly used in robotic systems, and thus displacement amplification is needed. Here we present a piezoelectric actuator that uses geometric amplification to achieve $20\times$ the nominal piezoelectric displacement. Actuator performance is described in terms of blocked force (20 mN), displacement (115 μm), bandwidth (3 kHz), and power density (172 W/kg). The actuator is fabricated using printed circuit MEMS, an emerging mesoscale manufacturing paradigm. Expected applications include locomotion for terrestrial crawling robots and flapping wing micro-air vehicles.**

I. INTRODUCTION

Actuator design and selection for mesoscale mechanical systems, which are typically defined as systems with characteristic lengths from hundreds of microns to several centimeters, remains an interesting problem in large part due to the behavior of scaling laws. On the mesoscale, the physics of scaling permit nearly any type of actuator: electromagnetic [1], [2], electrostatic [3], [4], piezoelectric [5], [6], shape-memory [7], [8], thermal-expansion [9], [10], and elastomeric [11] are all viable, and optimum actuator choice is not always clear. Typically, actuator choice is governed by properties such as power density, stroke, bandwidth, and force produced. Choice is also often governed by manufacturing concerns; producing high quality devices on the mesoscale is challenging, and a mixture of MEMS processes and conventional machining is typically used.

Piezoelectric-based actuators are an attractive option on the mesoscale for producing accurate, high-force, high-bandwidth motion. Without amplification, the motion produced by piezolectric actuators is typically too small (several μm) to be useful in physical systems. Amplification methods include internal leveraging (converting longitudinal strain to bending or twisting, i.e., bimporhs [12], unimporphs [13], [14], spiral actuators [15]), frequency leveraging [16], [17], and external leveraging [18], [19]. Either of the latter two methods can be used for amplifying in-plane motion, but we favor the external amplification due to its simplicity and the

Peter York and Robert J. Wood are with the School of Engineering and Applied Sciences, Harvard University, Cambridge, MA USA, pyork@g.harvard.edu, rjwood@eecs.harvard.edu
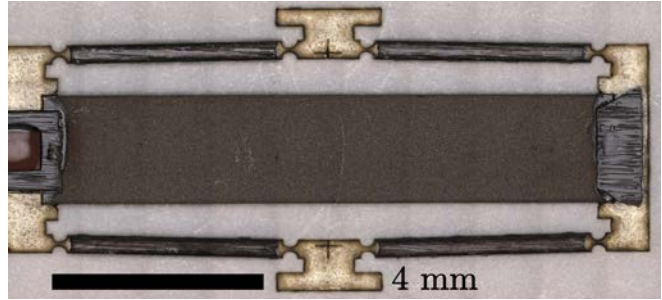

Fig. 1: Miniature amplified in-plane piezoelectric actuator. The carbon fiber/FR4 linkages amplify the longitudinal contraction of the PZT member by $20\times$. Circular flexure hinges are used to produce rotational motion at the linkage joints. Device thickness is $\sim$200 μm.

relative complexity of friction-based frequency amplification techniques.

Thus, we describe an externally amplified, in-plane piezoelectric actuator to be used in mesoscale robotic systems in which medium force, medium displacement motion is needed in a flat, compact profile (see Fig. 1). It consists of bulk piezoelectric ceramic (PZT-5H) surrounded by an FR4 frame with flexure hinges that amplify the in-plane contractional motion of the piezoceramic. Rigidity is enhanced by resin-impregnated carbon fiber on the front and back sides of the frame. It can be directly embedded in devices produced through printed circuit MEMs (PC-MEMs), a recently developed manufacturing paradigm that combines laser micromachining and multi-material lamination [20], [21], and similar manufacturing processes, or it can be used as a component in pick-and-place assemblies.

Our device is similar to the "Moonie" [18] and "Cymbal" [19] actuators, which were among the first piezoelectric actuators to utilize geometric amplification from an external frame. However, those devices and most that followed [22], [23] used the d_{33} mode of stacked piezoceramics as the fundamental actuation unit, whereas we use a single piece of piezoceramic in its d_{31} mode. Our device is most similar to the MEMS actuator [24], which uses thin-film PZT in the d_{31} mode to produce in-plane motion with a $10\times$ geometric amplification factor (the ratio of piezoelectric motion to output motion). Our device is different in terms of scale, manufacturing method, materials used, and ultimately shows better performance in terms of amplification factor ($20\times$).

II. DESIGN

The basic design of the actuator consists of a piezoceramic bonded to an external frame that geometrically amplifies the motion produced when an electric field is applied through the thickness of the piezoceramic. The key design parameters are
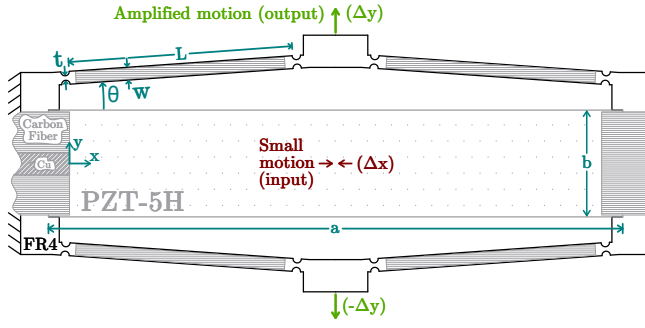
(a) Design schematic of the amplified linear actuator along with geometric parameters and principle of operation (top view). Small strains in the piezoceramic are transmitted through the flexure hinges and linkage arms to produce amplified motion at the output links. The piezoceramic is bonded to the frame using resin-impregnated carbon fiber. Electrical signals are applied through copper bonded to the top of the carbon fiber. The device has top-bottom and front-back symmetry.
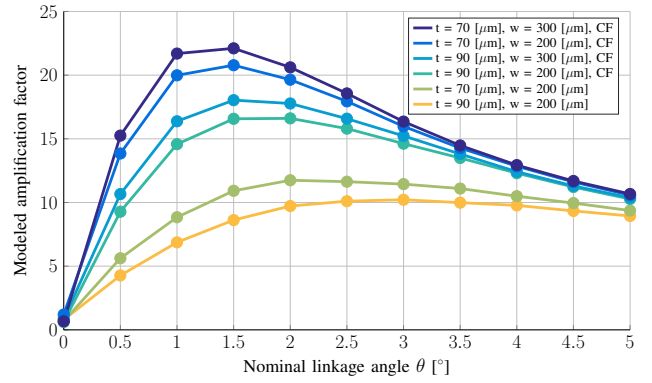
(b) Modeled amplification factor as a function of geometry and materials. The nominal linkage angle represents the initial configuration of the mechanism with respect to the singular configuration. Decreasing the flexure hinge thickness (t) increases the amplifcation factor, as do increasing the arm width (w) and adding carbon fiber reinforcements on the arms (CF). The amplification factor is nominally symmetric about the singular configuration for all device designs.

Fig. 2: Design of the amplified piezoelectric actuator

shown in Fig. 2a. The designer is free to choose the size of the piezoceramic, the size and nominal angle of the linkage arms, and the flexure thickness. We chose to use circular flexure hinges, though it could be advantageous to consider other geometries.

Material selection was governed by a variety of considerations. We chose to use PZT-5H (Piezosystems, USA) because of its high strain constants, in particular, d_{31}. We used QA-112, a high modulus, unidirectional pre-preg carbon fiber (Toho Tenax, Japan), because of its high modulus. For the frame, which includes the flexures, we chose to use FR4, a woven-fiber/resin composite, for its high strength-to-modulus ratio and its thermal stability at the cure temperature (150 °C) of the QA-112 resin. Finally, we added copper layers to provide a low resistivity path for the drive signal.

Our primary design goal was to maximize the amplification factor, which we define as the ratio of the output displacement of the mechanism and the contraction of the piezoelectric member:

$$\lambda = \lambda_A + \lambda_B = 2\frac{\Delta y}{\Delta x} \qquad (1)$$

as shown in Fig. 2a, where λ_A and λ_B are the amplification ratios of the top and bottom halves of the actuator, respectively. If the flexures at the joints of the mechanism are assumed to be perfectly compliant (i.e., revolute joints) and the links to be perfectly rigid, the amplification factor simply becomes:

$$\lambda = \cot\theta \qquad (2)$$

	PZT-5H	QA-112	FR4
Elastic modulus [GPa]	60	170 (0°), 10 (90°)	22
Thickness [um]	127	30	127
d_{31} [V/m]	-320×10^{-12}	–	–

TABLE I: Material properties used in finite element model. Note that the modulus and d_{31} constant of PZT-5H are in general field and strain dependent.

where θ is the nominal angular offset of the mechanism from its singular configuration. This relationship represents an upper bound on the amplification factor for the quasi-static case.

When joint and link stiffness are considered, determining the amplification factor becomes more challenging; the kinematics problem turns into a mechanics problem, which we solved using a commercial finite element package (COMSOL Multiphysics 4.4). The material properties used in the simulation are shown in Table I. Linear elastic deformation was assumed, and the coupled piezoelectric/solid-mechanics problem was solved for varying applied voltages and frequencies. Amplification factor was found to be nearly constant across voltage and frequencies in the actuator passband.

The results of the model for a variety of actuator designs are shown above in 2b. We held piezoceramic size (a, b) and linkage arm length (L) constant and varied nominal linkage angle (θ), flexure thickness (t), linkage arm width (w) and the presence of carbon fiber reinforcement on the linkage arms. For each design, we see a peak in the amplification ratio for some $\theta > 0$; these are the optimized geometries we are interested in selecting for a final design. In Fig. 2b, we also see that decreasing the flexure thickness (t) increases the amplification factor and that increasing the linkage arm width (w) moderately increases the amplification ratio. Finally, we see a large performance improvement when we add carbon fiber reinforcements to the top and bottom of the linkage arms.

We heuristically set a lower bound on flexure thickness at 70 μm due to several concerns: first, the gap between fiber bundles in the FR4 is relatively large (50 μm); second, the accuracy of the fabrication method used was ~10 μm; and third, extremely thin flexures were to be avoided to prevent buckling under load. Thus, we chose to manufacture the design represented by the maximum in Fig. 2b. This displacement-optimized design has a nominal linkage angle
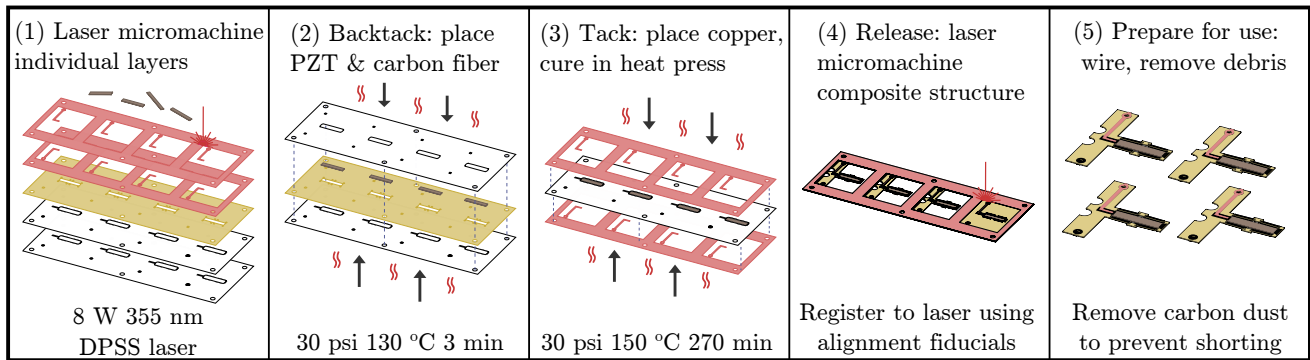
(1) Laser micromachine individual layers	(2) Backtack: place PZT & carbon fiber	(3) Tack: place copper, cure in heat press	(4) Release: laser micromachine composite structure	(5) Prepare for use: wire, remove debris
8 W 355 nm DPSS laser	30 psi 130 °C 3 min	30 psi 150 °C 270 min	Register to laser using alignment fiducials	Remove carbon dust to prevent shorting

Fig. 3: PC-MEMS process workflow. The process is easily parallelized for batch manufacturing.

of 1.5°, flexure thickness of 70 μm, linkage arm width of 300 μm, and contains carbon fiber reinforcements.

Output blocked force was also solved for using our finite element model, with the modeled force shown for our final design in Fig. 6. The force determined by the finite element model was corrected using the substitution $Ed_{31} \leftrightarrow f_{31}$, where f_{31}, as defined in [25], accounts for material nonlinearities in the piezoceramic at high fields and strains.

III. MANUFACTURING

The proposed design is straightforward to manufacture using a PC-MEMS manufacturing process, which in this case incorporates laser micromachining and pin-aligned heat/pressure lamination. An overview of the process is shown above in Fig. 3 and is explained in detail as follows:

(1) We begin by fabricating individual layers of PZT-5H, FR4, paper-backed resin-impregnated carbon fiber, and copper using laser micromachining. A 355-nm 8-W pulsed laser system is used (Oxford Lasers E Series). The laser spot size is power dependent and ranges from 7 to 20 μm and the position accuracy ranges from 5 to 15 μm. Care is taken to minimize chemical composition change of the piezoceramic during laser processing, which occurs during melting and resolidification of the material and results in reduced dielectric strength, as described in [25]. In practice, this means using several thousand cut passes at a relatively low laser power (0.23 W at 20 kHz pulse rate) to limit melting of the piezoceramic. Alternatively, one could use micropowder blasting to cut the piezoceramic, as in [26], which would obviate the possibility of thermal damage; however, downsides of the technique exist, namely etch anistropy and the need for extra process steps (photolithographic masking).

The paper-backed carbon fiber is processed using two steps: first, a low power cut through the carbon fiber that defined the desired final geometry, and second, a high power cut through the carbon fiber and the paper backing to create alignment holes and voids over regions in which resin flow was undesirable. The carbon fiber that was not part of the final geometry was subsequently peeled off of the paper backing.

(2) Next we place the 8.5×1.5 mm piezoceramic beams into slots in the FR4 layer and use alignment holes to mate the carbon fiber layers on the top and bottom of the

FR4 layers. The structure is then partially cured (30 psi, 150°C, 3 min) to transfer the carbon fiber from its paper backing to the FR4. This is a key step that allows carbon fiber to be placed only where desired. It is important for three reasons: first, by minimizing the amount of carbon fiber used, unwanted resin flow onto the piezoceramic or the to-be-created flexure joints can be avoided; second, it is critical to avoid cutting carbon fiber during the release cut (step 4, below), because the ablation process releases carbon dust that binds to the substrate edges, shorting the device; third, because mismatch between the top and bottom layer of carbon fiber can cause warping in the laminate during curing, putting stress on the piezoceramic. Minimizing the amount of carbon fiber can minimize this effect. During the carbon fiber transfer process, compressible (Pacothane Technologies PACOPADS) and chemical resistant layers (FEP) were added to ensure a uniform pressure distribution and minimize resin flow, respectively.

(3) Following the carbon fiber transfer process, we peel off the paper backing and mate the copper layers to the revealed carbon fiber/FR4/carbon fiber laminate. The structure was fully cured (30 psi, 150°C max, 270 min), once again with the temporary addition of compressible and chemically resistant layers.
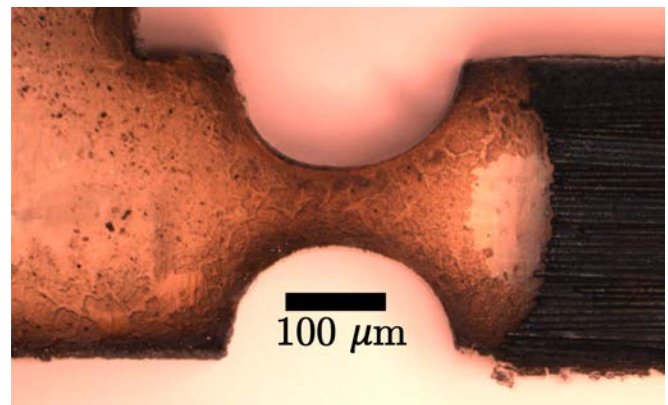

Fig. 4: Circular flexure hinge (center) and carbon fiber reinforced linkage arm end (right) created during laser micromachining release cut.

(4) After the laminate is cured, we register it to the laser micromachining system using alignment fiducials and cut
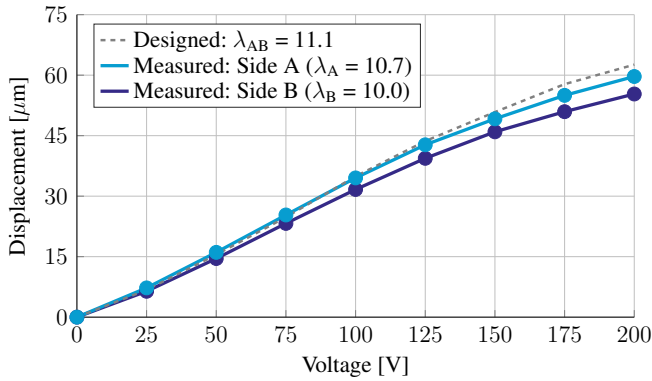
Fig. 5: Output link displacement vs. applied voltage (quasi-static). The designed displacement was based on our amplification ratio model and on measurements of the actual displacement of the piezoelectric beam. The nonlinear response is due to the nonlinearity of piezoelectric electromechanical coupling with respect to applied field.

the final geometry of the device. This is the step in which the amplification mechanism is formed; care is taken to cut the fine features of the mechanism (the flexure hinges and linkage arms) before fully releasing the structure. Low power is used to minimize laser spot size and avoid thermal damage to the laminate, in particular, the FR4. A zoomed-in image showing a fabricated flexure is shown in Fig. 4.

(5) After the actuator is released from the substrate, it is cleaned with isopropyl alchohol to remove any carbon dust deposited during laser ablation. We typically place the actuators in an 80 °C ultrasonic bath for 5 min. Removing the carbon dust minimizes the risk of electrically shorting and is especially important for high-field operation. Finally, the actuator is wired and prepared for testing and/or integration into robotic devices.

IV. CHARACTERIZATION

The manufactured geometry closely matched the designed geometry (see Table II), though there is room for improvement. In particular, we found that there was some asymmetry between the two halves of the actuator. Measurements were taken using a confocal microscope (Olympus OLS 4000).

	linkage angle θ [°]	flexure thickness t [μm]
Designed	1.5	[70, 70, 70, 70]
Side A	1.8	[78, 78, 61, 61]
Side B	2.0	[85, 81, 81, 57]

TABLE II: Designed vs. produced geometry. Side A and Side B denote the two halves of the amplification mechanism (bottom and top halves, respectively, of the actuator in Fig.1). We see some discrepancy between designed and produced geometry and slight deviation between the two sides.

The output displacement vs applied voltage characteristic is shown above in Fig. 5. We see that both sides of the actuator slightly deviate from the designed behavior, though, given the geometry actually produced, both sides match well the model predictions in Fig. 2b. Measurements were taken with a laser Doppler vibrometer (Polytec PSV-500) with the actuator driven at 200 Hz, which is well within the bandwidth of the actuator and results in reasonably large velocities ($\sim$1-
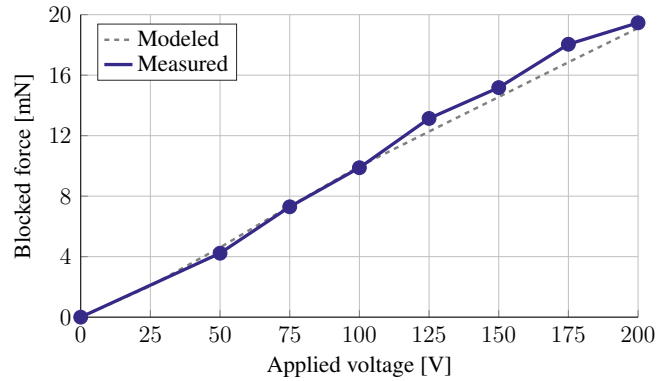

Fig. 6: Applied force vs. applied voltage (quasi-static (1 Hz) sinusoidal input).

50 mm/s) that are well above the noise floor of the vibrometer ($\sim$50 μm/s for these tests).

The frequency response of the actuator was measured using the vibrometer and the results are shown below in Fig. 8. White noise was used to stimulate the actuator. We see the expected second-order response for the system, with its resonance at 4.25 kHz. The passband displacement amplitude is $\sim$360 nm/V, which is consistent with the displacement measurements for low frequencies taken above. The phase swing slightly above 3 kHz is likely due to the slight asymmetry between the two sides of the actuator.

Actuator blocked force was measured using the testbed shown in Fig. 7. The actuator and test probe were mounted on linear stages to allow for precise alignment with the force sensor (an ATI Nano 17). The actuator was positioned such that its linkages were undeformed at zero applied voltage and kept in this position for all tests. Measurements were taken across a range of applied voltages and are shown in Fig. 6. We see that the measured blocked force closely matches our model.

Finally, we conducted a preliminary fatigue test and found that the actuator was able to complete 40,000 cycles under free displacement without failure when driven by a 3 kHz sinusoidal signal at 100 V.
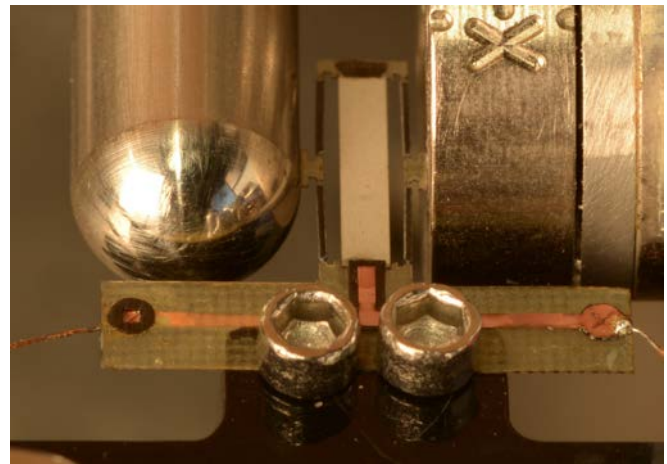

Fig. 7: Actuator blocked force testbed. Actuator is shown in the center with the force sensor on the right. The probe on the left was used to mechanically ground the actuator.
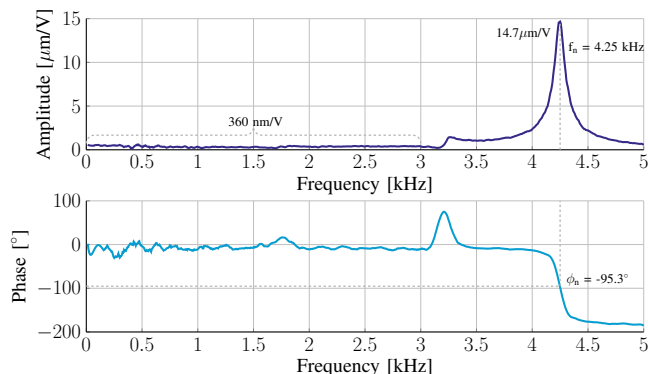
Fig. 8: Frequency response of the actuator.

V. DISCUSSION

Our experimental results show good agreement with our models for amplification factor and blocked force. They also illustrate the need to reduce manufacturing variance, which could be accomplished by using the same region of the laser micromachining system's galvo scanner for cutting each flexure and linkage arm (accuracy varies throughout the galvo field).

At 200 V, free deflection, blocked force, and bandwidth were measured to be 115 μm, 20 mN, and 3 kHz, respectively. Given a mass of 20 mg, the actuator power density is determined to be 172 W/kg. It is likely that the power density optimized design is not the same as the displacement optimized design determined and presented here, and future work could include exploring power density optimization. To increase output force, different flexure geometries could be considered. Also, the incorporation of hard stops could increase output force and prevent buckling under load.

There are other interesting design possibilities. The output motion of the device includes a small component in the orthogonal in-plane direction; this motion could be minimized by using slightly different linkage arm lengths within a single side (though this does result in small rotations at the output link). Rounded cantilever flexures could improve fatigue life by more uniformly distributing stress, but they would likely also lead to higher off-axis compliance, which would lead to lower force output. A parylene coating step would reduce the risk of dielectric breakdown and allow the actuator to be safely operated at higher voltages.

Note that this actuator could be made across a range of scales. The lower bound on actuator size would likely be heavily influenced by the position accuracy of the laser micromachining system ($\sim$10 μm). The actuator could be made arbitrarily large, but it becomes a less attractive option relative to electromagnetic drives as its size increases.

VI. CONCLUSION

We have presented a new piezoelectric actuator for mesoscale robotic systems. It uses geometric amplification to magnify the displacement of a single piezoceramic beam. A model for amplification ratio was provided for a variety of design conditions and was shown to be valid for a displacement-optimized design, which demonstrates an amplification factor of 20$\times$. A blocked force model for the optimized design was also presented and validated. Finally, a manufacturing process for fabricating the actuators was described in detail, and suggestions for improvements of the actuator were provided.

VII. ACKNOWLEDGMENTS

REFERENCES

[1] P. Zhang and Q. Zhou, "Voice coil based hopping mechanism for microrobot," in *IEEE International Conference on Robotics and Automation, 2009*, pp. 3001–3006.
[2] B. Goldberg, M. Karpelson, O. Ozcan, and R. J. Wood, "Planar fabrication of a mesoscale voice coil actuator," in *IEEE International Conference on Robotics and Automation, 2014*, pp. 6319–6325.
[3] D. A. Horsley, M. B. Cohn, A. Singh, R. Horowitz, and A. P. Pisano, "Design and fabrication of an angular microactuator for magnetic disk drives," *Journal of Microelectromechanical Systems*, vol. 7, no. 2, pp. 141–148, 1998.
[4] B. R. Donald, C. G. Levey, C. D. McGray, I. Paprotny, and D. Rus, "An untethered, electrostatic, globally controllable mems micro-robot," *Journal of Microelectromechanical Systems*, vol. 15, no. 1, pp. 1–15, 2006.
[5] A. M. Flynn, L. S. Tavrow, S. F. Bart, R. A. Brooks, D. J. Ehrlich, K. R. Udayakumar, and L. E. Cross, "Piezoelectric micromotors for microrobots," *Journal of Microelectromechanical Systems*, vol. 1, no. 1, pp. 44–51, 1992.
[6] S. Koganezawa, Y. Uematsu, T. Yamada, H. Nakano, J. Inoue, and T. Suzuki, "Dual-stage actuator system for magnetic disk drives using a shear mode piezoelectric microactuator," *IEEE Transactions on Magnetics*, vol. 35, no. 2, pp. 988–992, 1999.
[7] D. Reynaerts, J. Peirs, and H. Van Brussel, "Shape memory microactuation for a gastro-intestinal intervention system," *Sensors and Actuators A: Physical*, vol. 77, no. 2, pp. 157–166, 1999.
[8] M. Noh, S.-W. Kim, S. An, J.-S. Koh, and K.-J. Cho, "Flea-inspired catapult mechanism for miniature jumping robots," *IEEE Transactions on Robotics*, vol. 28, no. 5, pp. 1007–1018, 2012.
[9] M. Ataka, A. Omodaka, N. Takeshima, and H. Fujita, "Fabrication and operation of polyimide bimorph actuators for a ciliary motion system," *Journal of Microelectromechanical Systems*, vol. 2, no. 4, pp. 146–150, 1993.
[10] Y. Yamagata, T. Higuchi, N. Nakamura, and S. Hamamura, "A micro mobile mechanism using thermal expansion and its theoretical analysis. a comparison with impact drive mechanism using piezoelectric elements," in *IEEE Workshop on Micro Electro Mechanical Systems, 1994.*, pp. 142–147.
[11] M. Duduta, R. J. Wood, and D. R. Clarke, "Multilayer dielectric elastomers for fast, programmable actuation without prestretch," *Advanced Materials*, 2016.
[12] R. Wood, E. Steltz, and R. Fearing, "Optimal energy density piezoelectric bending actuators," *Sensors and Actuators A: Physical*, vol. 119, no. 2, pp. 476–488, 2005.
[13] K.-J. Yoon, K.-H. Park, S.-K. Lee, N.-S. Goo, and H.-C. Park, "Analytical design model for a piezo-composite unimorph actuator and its verification using lightweight piezo-composite curved actuators," *Smart Materials and Structures*, vol. 13, no. 3, p. 459, 2004.
[14] K. R. Oldham, J. S. Pulskamp, R. G. Polcawich, and M. Dubey, "Thin-film pzt lateral actuators with extended stroke," *Journal of Microelectromechanical Systems*, vol. 17, no. 4, pp. 890–899, 2008.
[15] F. Mohammadi, A. Kholkin, B. Jadidian, and A. Safari, "High-displacement spiral piezoelectric actuators," *Applied Physics Letters*, vol. 75, no. 16, pp. 2488–2490, 1999.
[16] T. Morita, "Miniature piezoelectric motors," *Sensors and Actuators A: Physical*, vol. 103, no. 3, pp. 291–300, 2003.
[17] D. Henderson, "Simple ceramic motor... inspiring smaller products," *International Conference on New Actuators*, vol. 50, no. 10, 2006.

[18] R. Newnham, A. Dogan, Q. Xu, K. Onitsuka, and S. Yoshikawa, "Flex-tensional moonie actuators," in *Ultrasonics Symposium, Proceedings.* IEEE, 1993, pp. 509–513.

[19] A. Dogan, K. Uchino, and R. E. Newnham, "Composite piezoelectric transducer with truncated conical endcaps 'cymbal'," *Ultrasonics, Ferroelectrics, and Frequency Control, IEEE Transactions on*, vol. 44, no. 3, pp. 597–605, 1997.

[20] P. S. Sreetharan, J. P. Whitney, M. D. Strauss, and R. J. Wood, "Monolithic fabrication of millimeter-scale machines," *Journal of Micromechanics and Microengineering*, vol. 22, no. 5, 2012.

[21] J. Whitney, P. Sreetharan, K. Ma, and R. Wood, "Pop-up book mems," *Journal of Micromechanics and Microengineering*, vol. 21, no. 11, 2011.

[22] J. Ueda, T. W. Secord, and H. H. Asada, "Large effective-strain piezoelectric actuators using nested cellular architecture with exponential strain amplification mechanisms," *IEEE/ASME Transactions on Mechatronics*, vol. 15, no. 5, pp. 770–782, 2010.

[23] C. Technologies. (2014, November) Apa30uxs. [Online]. Available: http://www.cedrat-technologies.com/fileadmin/user_upload/cedrat_groupe/Mechatronic_products/Piezo_actuators_electronics/APAs/Technical_Datasheet/APA30XS_GB_v4.0.pdf

[24] N. J. Conway and S.-G. Kim, "Large-strain, piezoelectric, in-plane micro-actuator," in *17th IEEE International Conference on Micro Electro Mechanical Systems*, 2004, pp. 454–457.

[25] N. T. Jafferis, M. J. Smith, and R. J. Wood, "Design and manufacturing rules for maximizing the performance of polycrystalline piezoelectric bending actuators," *Smart Materials and Structures*, vol. 24, no. 6, 2015.

[26] I. Misri, P. Hareesh, S. Yang, and D. DeVoe, "Microfabrication of bulk pzt transducers by dry film photolithography and micro powder blasting," *Journal of Micromechanics and Microengineering*, vol. 22, no. 8, 2012.